AAS 23-200

REPHASING AND LOITERING STRATEGIES IN THE GATEWAY NEAR RECTILINEAR HALO ORBIT

Brian McCarthy,[*] Stephen Scheuerle,[†] Emily Zimovan-Spreen,[‡] Dale Williams,[§] Diane Davis[¶] and Kathleen Howell[‖]

NASA's Gateway plans to operate in an L_2 9:2 lunar synodic resonant Near Rectilinear Halo Orbit (NRHO) for nominal operations. During the mission's lifetime, scenarios may arise where rephasing within the NRHO or loitering in an alternate trajectory are advantageous. This investigation discusses two strategies to perform this rephasing in the NRHO over a relatively short timespan. The first method uses two maneuvers to shift the phase along a single transfer arc. The second strategy employs four maneuvers, leveraging an intermediate orbit for rephasing. An optimization strategy is formulated to construct locally optimal solutions in the Circular Restricted Three-Body Problem (CR3BP) and verified in a higher-fidelity ephemeris model.

INTRODUCTION

In November 2022, the Artemis 1 mission launched to test the Orion crew capsule, kicking off the first component of the campaign to develop a sustaining human presence in cislunar space.[1] One aspect of this campaign is development of the lunar Gateway station, which seeks be a testbed for sustaining humans in deep space. The Gateway station plans to operate in an Earth-Moon southern L_2 Near Rectilinear Halo Orbit (NRHO) which has a 9:2 lunar synodic resonance. This resonance provides that, for every 9 revolutions with a spacecraft in the orbit, two synodic periods of the Moon are completed. The characteristics of this operational orbit provide natural eclipse avoidance properties while balancing feasible access to the lunar surface and other locations in deep space. Given the unique dynamical environment surrounding the 9:2 NRHO, knowledge of nearby dynamical structures is necessary for Gateway mission operations. In this investigation, characteristics of the NRHO and motion in the vicinity are examined as applied to loitering near and rephasing in the 9:2 NRHO. Understanding the rephasing and loitering problem for the Gateway is beneficial for flexibility in visiting vehicle opportunities, lunar surface missions, eclipse and derbis avoidance, and cubesat deployment. Several strategies are summarized in this investigation to understand the maneuver costs and times-of-flight associated with various duration phase shifts.

Several previous investigations have examined relative motion, rephasing, and loitering trajectories in the vicinity of NRHOs. Khoury and Howell examined loitering applications in the vicinity of a 9:2 NRHO in the Circular Restricted Three-Body Problem (CR3BP).[2] Sandel and Sood examined proximity operations and rendezvous for a low-thrust spacecraft in an NRHO.[3] Additionally, Davis et al. examined a process to shift the phase within a 9:2 NRHO using the nominal Gateway stationkeeping algorithm in an ephemeris model over several months.[4] Rendezvous design was also examined by Blazquez et al. in an ephemeris model.[5] Bucchioni et al. examined different phasing orbit configurations and leveraged manifold trajectories for cargo vehicles in the vicinity of the 9:2 NRHO in the CR3BP.[6] This investigation aims to develop several strategies

---

[*] Gateway Mission Design Engineer, a.i. solutions, Inc.; brian.p.mccarthy@nasa.gov

[†] Ph.D. Student, Purdue University; ssheuer@purdue.edu

[‡] Gateway Mission Design Engineer, NASA JSC; emily.m.spreen@nasa.gov

[§] Graduate Student, Purdue University; will1738@purdue.edu

[¶] Gateway Mission Design Engineer, NASA JSC; diane.c.davis@nasa.gov

[‖] Hsu Lo Distinguished Professor of Aeronautics and Astronautics, Purdue University; howell@purdue.edu to move Gateway or visiting vehicles in the vicinity of the 9:2 NRHO over a relatively brief timespan. The term phase in this analysis relates a specific location on the orbit to a given epoch. Moving from one phase to another is advantageous for rendezvous, cubesat deployment, and eclipse avoidance. Whereas, for mitigating conjunctions with debris or visiting vehicles, the aim is to depart from the reference trajectory but return to the original phase. This investigation seeks to address several methods to depart the Gateway's nominal NRHO, then return at the same phase along the original baseline, or to a different phase along a new baseline trajectory. Two rephasing methods are presented to increase flexibility for rephasing and loitering that are achievable within one or several NRHO revolutions. First, a two-burn rephasing strategy is presented in which, for a given rephasing duration, a single maneuver is performed to depart the original baseline NRHO and a single maneuver is performed arrive on a new, phase-shifted baseline. The second rephasing method leverages an intermediate phasing orbit and four maneuvers. A phasing orbit is chosen and sized such that the proper rephase duration on the NRHO is achieved. In the course of the analysis, an optimization technique is summarized and paired with pseudo-arclength continuation to construct families of locally optimal solutions. These rephasing strategies offer flexibility in performing operations in and around the vicinity of the Gateway NRHO.

DYNAMICAL MODELS

Two dynamical models are leveraged in this investigation, the Circular Restricted Three-Body Problem (CR3BP) and a Sun-Earth-Moon ephemeris model. The CR3BP offers higher fidelity and additional behaviors in comparison to the two-body model. In this model, two gravitational bodies, denoted P_1 and P_2, remain in circular Keplerian orbits about their mutual barycenter (i.e., center of mass). A third body, P_3, moves under the gravitational influence of the two larger bodies and is assumed to be massless. The model is defined relative to a rotating coordinate system, where the $+\hat{x}$ direction is defined from the barycenter toward P_2. The $+\hat{z}$ direction is defined parallel to the direction of the orbital angular momentum vector for P_1 and P_2; the $\hat{y}$ direction completes the orthonormal triad. The position and velocity of P_3 relative to the barycenter in the rotating frame are defined as $\vec{x} = \begin{bmatrix} x & y & z & \dot{x} & \dot{y} & \dot{z} \end{bmatrix}^T$, where the first three and the last three elements are the position and relative velocity components, respectively. The equations of motion for a particle moving in the CR3BP are a set of three, second-order scalar differential equations of motion,

$$\ddot{x} - 2\dot{y} = \frac{\partial U^*}{\partial x} \qquad \ddot{y} + 2\dot{x} = \frac{\partial U^*}{\partial y} \qquad \ddot{z} = \frac{\partial U^*}{\partial z} \tag{1}$$

The pseudo-potential is a scalar defined solely as a function of position and the CR3BP mass parameter, $\mu = M_2/(M_1 + M_2)$, where M_1 and M_2 are the masses of P_1 and P_2, respectively.[7] The pseudo-potential function takes the following form,

$$U^* = \frac{x^2 + y^2}{2} + \frac{\mu}{r} + \frac{1-\mu}{d} \tag{2}$$

where $d = \sqrt{(x+\mu)^2 + y^2 + z^2}$ and $r = \sqrt{(x-1+\mu)^2 + y^2 + z^2}$ represent the distances of P_3 relative to P_1 and P_2, respectively. The CR3BP admits a single integral of the motion, commonly denoted the Jacobi Constant (JC). The Jacobi Constant is a function of the pseudo-potential and the relative velocity magnitude expressed in the rotating reference frame,

$$JC = 2U^* - v^2 \tag{3}$$

where $v = \sqrt{\dot{x}^2 + \dot{y}^2 + \dot{z}^2}$. The Jacobi Constant is an energy-like quantity that characterizes motion in a CR3BP system and remains constant for all time over any ballistic arc propagated in the CR3BP. One advantage of the CR3BP model is that the system is time invariant. The CR3BP is a good approximation for a multi-body environment and the trajectory characteristics generally persist when transitioning results to a higher-fidelity ephemeris model.

The ephemeris force model offers a higher-fidelity gravity force representation on the spacecraft by incorporating the ephemeris states of various celestial bodies. For this investigation, the ephemeris model includes the Sun and Earth as point masses, and an 8 × 8 lunar gravity field. The interpolated position and velocity state corresponding to these bodies are extracted from the ephemerides on the JPL NAIF server.[8] The propagation, targeting and visualization in this model are performed using Freeflyer. The analysis performed in the ephemeris model reinforces the result found in the CR3BP and represents a more realistic cislunar environment to execute this scenario for a real mission.

CONTINUATION OF LOCALLY OPTIMAL SOLUTIONS

In this investigation, families of solutions are assessed in the CR3BP to understanding the fundamental motion associated with performing rephasing in the NRHO. Subsequently, an algorithm is developed to construct these families of solutions. Consider a free-variable/constraint formulation of a differential corrections problem where $\bar{X}$ is defined as the free-variable vector,

$$\bar{X} = \begin{bmatrix} x_1 & x_2 & \dots & x_n \end{bmatrix}^T \tag{4}$$

and where x_i is the i^{th} free-variable and there are n free-variables. The constraint vector, $\bar{F}$ is defined,

$$\bar{F} = \begin{bmatrix} F_1 & F_2 & \dots & F_{n-2} \end{bmatrix}^T = \bar{0} \tag{5}$$

where F_i is the i^{th} scalar constraint. Additionally, a constraint is formulated to minimize or maximize a cost function and is appended to the end of the constraint vector, making $n-1$ constraints,

$$F_{opt} = \nabla f \bullet \text{null}\left(D\bar{F}\right) = 0 \tag{6}$$

where ∇f is the gradient of the cost function to be minimized or maximized, null$(D\bar{F})$ is the nullspace of $D\bar{F}$, where $D\bar{F}$ is defined,

$$D\bar{F}_a = \begin{bmatrix} \frac{\partial F_1}{\partial x_1} & \cdots & \frac{\partial F_1}{\partial x_{n-1}} \\ \vdots & \ddots & \vdots \\ \frac{\partial F_{n-2}}{\partial x_1} & \cdots & \frac{\partial F_{n-2}}{\partial x_{n-1}} \end{bmatrix} \tag{7}$$

which is a submatrix of the Jacobian matrix for the differential corrections problem defined by Equations (4) and (5). Note that the matrix defined in Equation (7) does not include the partial derivatives with respect to the last variable in the free-variable matrix, x_n. This variable is chosen depending on the problem and is discussed in subsequent sections. Setting up an optimization in this manner is a reformulation of constrained optimization using Lagrange multipliers, but removes the need to solve for the Lagrange multipliers and their associated costate equations. A proof for how this formulation is related to a formulation using Lagrange multipliers is summarized in the Appendix. By appending the optimality constraint to the constraint vector, the differential corrections problem possesses $n-1$ constraints and n free-variables. Subsequently, a pseudo-arclength continuation process is implemented to generate a family of solutions.[9,10] The final constraint vector is defined,

$$\bar{F}_a = \begin{bmatrix} F_1 & F_2 & \dots & F_{n-2} & F_{opt} & F_{PAL} \end{bmatrix}^T = \bar{0} \tag{8}$$

where F_{PAL} is the pseudo-arclength constraint. Note that a second-derviative constraint to ensure that the cost function is minimized or maximized is not included in this formualation. Subsequently, the first solution computed in the family must be evaluated to ensure that the cost function is minimized/maximized.

To demonstrate the optimization technique paired with pseudo-arclength continuation visually, consider a problem that has parameters p_1 and p_2 that represent the solution space. The feasible solution space encompasses all parameters p_1 and p_2 that satisfy some set of constraints and are used to define a cost function, $f(p_1, p_2)$. The cost function is plotted to show all of the feasible solutions as a 2-dimensional surface in Figure 1. Using the optimality constraint and the continuation process described in this section, a family of 1-parameter optimal solutions is computed that is represented by the red dots, along the “valley” of the surface in Figure 1. The algorithm uses pseudo-arclength continuation to produce members of the family, which is more robust to changes in the parameters of the problem, as it enforces a constraint that requires each member to be on the family of solutions and is independent of the changes in any of the parameters. For example, if natural parameter continuation is used to generate the family of solutions along the red curve in

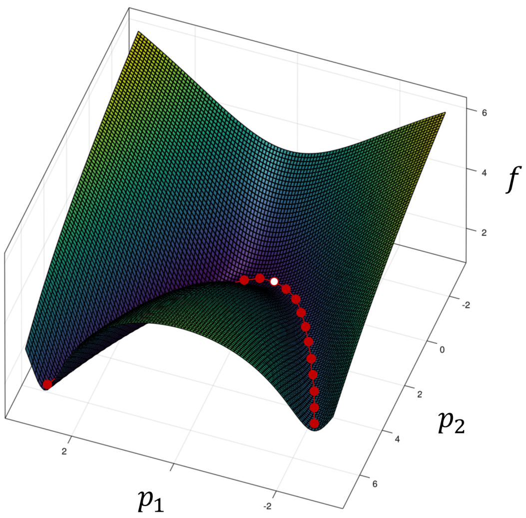

Figure 1. Cost function plotted as a function of two parameters in the feasible solution space. The red line and dots correspond to a family of optimal solutions that minimize the cost function.

Figure 1, the continuation halts when it reaches a solution corresponding to the white point since there are no solutions along the family with a value of p_2 greater the solution associated with the white point. However, pseudo-arclength continuation follows the entirety of the family and does not stop when the curve reverses direction in parameter p_2. Using this formulation, families of solutions are developed in this investigation. This method to perform continuation and generate families of locally optimal solutions is more robust when paired with a pseudo-arclength strategy. While the feasible set of solutions for this investigation is also of interest, most of the feasible solutions are associated with Δv costs that are not practical for this application. Subsequently, this optimal continuation strategy allows construction of a more practical set of solutions and reduces the large feasible solution space down to a more useful set.

REPHASING STRATEGIES

Two rephasing strategies are examined in this investigation, a two-burn strategy and a four-burn strategy. The two-burn strategy provides a sufficient method for shorter rephasing durations that change the NRHO phase by up to two days. The two-burn strategy encompasses times of flight from several days up to two weeks. The four-burn rephasing strategy is a method to handle longer rephasing durations that adjust the NRHO phase by more than one day. The four-burn rephase strategy also typically requires longer times-of-flight, which are on the order of two weeks to one month. The rephasing duration is defined as the amount of time ahead or behind the nominal phase. For example, a phase duration of 12 hours behind means that a spacecraft in the new phase passes over perilune 12 hours after the nominal phase. These strategies are first evaluated in the CR3BP, then validated in the higher-fidelity ephemeris model. These rephasing strategies are intended to be shorter time-of-flight alternatives to the strategy developed by Zimovan-Spreen et al., which require times-of-flight on the order of months to complete rephasing.[11] Development of methods to rephase to any location along the 9:2 NRHO with various times-of-flight and maneuver magnitudes ensures greater flexibility in the overall Gateway mission architecture.

Two-Burn Rephasing Strategy

A method to perform phase changes on the order of several hours to two days is accomplished through a two-burn strategy. The two-burn phase change assumes the transfer incorporates two impulsive maneuvers. The departure maneuver causes the spacecraft to exit the original NRHO baseline and enter a transfer arc.

The arrival maneuver returns the spacecraft to a new baseline NRHO at the new desired phase. A diagram of the two-burn rephase is illustrated in Figure 2(a). After the departure maneuver, the spacecraft embarks onto a transfer arc, which connects the departure and arrival locations. The two-burn strategy is suitable for shorter rephase durations and requires shorter times-of-flight along the transfer segment of the rephase. First, a targeting strategy is developed in the CR3BP to construct transfer arcs that give insight into the fundamental motion. The goal is to obtain a desired phase shift with minimal propellant usage. For a given phase shift, varying the departure and arrival locations, as well as time-of-flight, enables a vast range of possible transfers. The optimal targeting strategy helps reduce the solution-space. There are nine free variables for the two-burn problem,

$$\bar{X} = \begin{bmatrix}\Delta\bar{v}_1 & \Delta\bar{v}_2 & \tau_1 & \tau_2 & t\end{bmatrix}^T \tag{9}$$

where $\Delta\bar{v}_1$ and $\Delta\bar{v}_2$ are the two vectors the describe the departure and arrival impulsive maneuvers, the term t is the time-of-flight of the transfer, and variables τ_1 and τ_2 defined the arrival and departure location along the NRHO as time past perilune. The graphic in Figure 2(b) illustrates the parameter τ along the NRHO as the time past perilune. To attain the target state on the NRHO, while performing the proper phase change, yields seven constraints on the problem. Incorporating the optimal targeting strategy provides an eighth equation, thus, the complete constraint vector is defined,

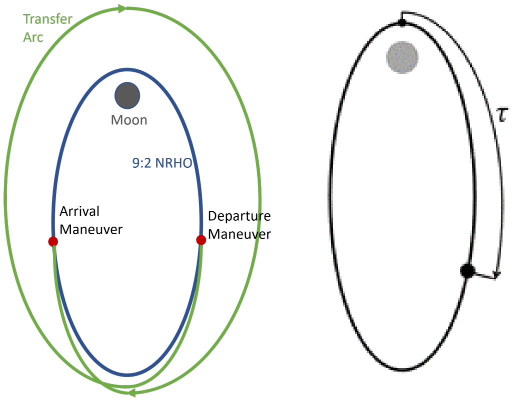

(a) (b)

Figure 2. (a) Two-maneuver rephase strategy diagram (not to scale). (b) Illustration demonstrating time since perilune.

$$\bar{F} = \begin{bmatrix} x_f - x_{\tau_2} \\ y_f - y_{\tau_2} \\ z_f - z_{\tau_2} \\ \dot{x}_f - \dot{x}_{\tau_2} - \Delta\dot{x}_2 \\ \dot{y}_f - \dot{y}_{\tau_2} - \Delta\dot{y}_2 \\ \dot{z}_f - \dot{z}_{\tau_2} - \Delta\dot{z}_2 \\ \tau_2 - \tau_1 - t - mT_p \\ F_{\text{opt}} \end{bmatrix} \tag{10}$$

where T_p is the period of the 9:2 NRHO, m is an integer value to define the number of revs around the NRHO, F_{opt} is defined in Equation (6), $\Delta\dot{x}_2$, $\Delta\dot{y}_2$, and $\Delta\dot{z}_2$ are the components of $\Delta\bar{v}_2$, $\dot{x}_{\tau_2}$, $\dot{y}_{\tau_2}$, and $\dot{z}_{\tau_2}$ are the velocity components of the target state on the NRHO, i.e., the state at τ_2, and $\dot{x}_f$, $\dot{y}_f$, and $\dot{z}_f$ are the velocity components at the end of the transfer arc. With nine free variables and eight constraints, the problem is underdetermined. Pseudo-arclength continuation is applied to continue along a family of optimal solutions. Consider a sample case where Gateway phase shifts 12 hours ahead within one revolution of the NRHO. A family of transfers is created in which each transfer achieves the local minimum propellant usage for the departure location on the NRHO. Three transfers from the family are illustrated in Figure 3(a), while the evolution of the maneuver cost and time-of-flight across the family are depicted in Figure 3(b). The yellow curve represents the baseline NRHO in the Earth-Moon rotating frame. The red, green, and blue dots in Figure 3(a) indicate the departure maneuver locations along the NRHO for each sample transfer. The red curve is a transfer with a time-of-flight of 3 days with a cumulative maneuver magnitude of 75.0 m/s. The green arc represents a trajectory with a flight duration of 4 days with a total maneuver magnitude of 53.1 m/s. The blue curve is a transfer with a time-of-flight of 5 days and a total maneuver magnitude of 40.6 m/s. Since these transfers pass on the inside of NRHO, as projected into the yz-plane, they are denoted ”interior” two-burn rephase transfers. This characteristic is common of transfers that shift the phase in positive time. The graph depicted in Figure 3(b) demonstrates how the departure, arrival, and cumulative maneuver cost evolves across the family of solutions. The dotted line is the first maneuver, which for most of the family is the more expensive maneuver. The dashed line is the second maneuver, and the solid line is the sum of the two maneuvers. For the 12-hour phase shift within one revolution of the NRHO, the minimum maneuver magnitude is 38.8 m/s, when the flight duration is 5.3 days.

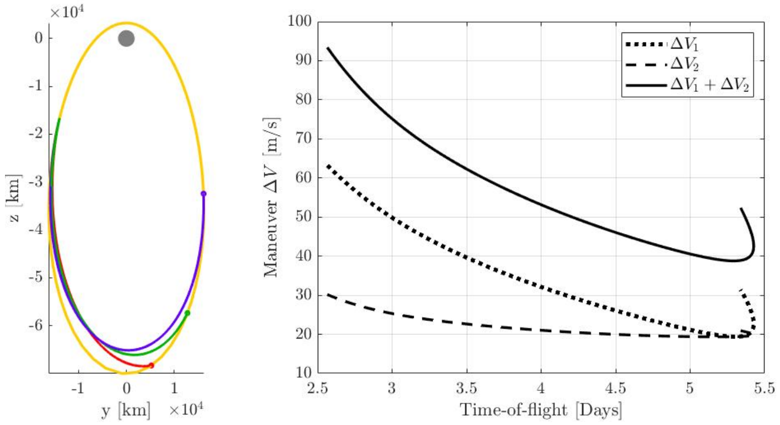

(a) (b)

Figure 3. Family of “interior” transfers that shift 12 hours forward in phase during one revolution of the NRHO, (a) illustrated in CR3BP in the Earth-Moon rotating frame, and (b) the evolution of the maneuver magnitude and time-of-flight along the family.

Similarly, a family of transfers is constructed to achieve transfers to a new NRHO phased 12 hours behind the original baseline. Three transfers from the family are illustrated in Figure 4(a), and the evolution of time-of-flight and maneuver cost are depicted in Figure 4(b). These transfers are denoted “exterior” transfers since they pass on the outside of the NRHO, as viewed in the yz-plane of the Earth-Moon rotating frame. The red curve has a time-of-flight of four days and a maneuver magnitude of 60.8 m/s. The green arc has a transfer duration of five days and a maneuver cost of 47.3 days. The blue arc has a time-of-flight of six days and a cumulative maneuver magnitude of 38.4 m/s. The external transfers in Figure 4(a) extend beyond the apolune of the original NRHO, and thus the transfers require more time to reach the arrival destination on the new NRHO. In contrast, the interior transfers in Figure 3(a) reduce the apolune distance to shorten the time-of-flight. Note that the optimal arrival location just prior to perilune on the NRHO remains approximately the same for the interior and exterior transfers, as seen in where the green, red, and purple transfer arcs terminate on the left side of the NRHO in Figures 3(a) and 4(a).

The departure location along the NRHO varies with the time-of-flight of the transfer which yields a variation in the cumulative maneuver magnitude. Note that for both the 12-hour ahead and 12-hour behind families, the minimum maneuver magnitudes are approximately 40 m/s. The propellant cost evolves with the desired phase shift. Consider a 24-hour phase shift behind in the NRHO, depicted as the red curve in Figure 5(a). This transfer is the propellant optimal solution with a flight time of 6.7 days and a cumulative maneuver

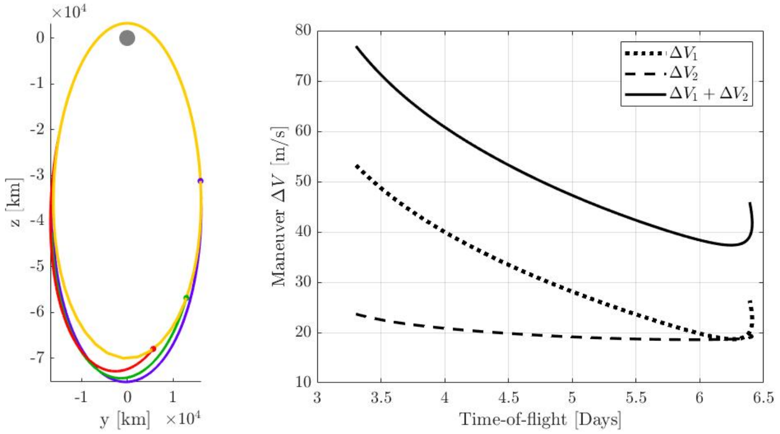

(a) (b)

Figure 4. Family of "exterior" transfers that shift 12 hours backward in phase during one revolution of the NRHO, (a) illustrated in the Earth-Moon rotating frame, and (b) the evolution of the maneuver magnitude and time-of-flight along the family.

cost of 73.7 m/s. The evolution of the maneuver magnitudes is illustrated in Figure 5(b). The increase in phase change from 12 to 24 hours results in higher propellant costs. Two additional families are generated, with a 48-hour phase shift ahead and behind in one revolution of the NRHO, Figure 6(a) and Figure 6(b), respectively. The transfer in Figure 5a has a flight duration of 3.9 days and cumulative maneuver cost of 167 m/s. The trajectory in Figure 5b has a time-of-flight of 7.7 days and a total maneuver magnitude of 144.7 m/s. Similar to the comparison between Figure 4(a) and Figure 5(a), the increased phase shift from 24 hours to 48 hours leads to an increase in the maneuver magnitude.

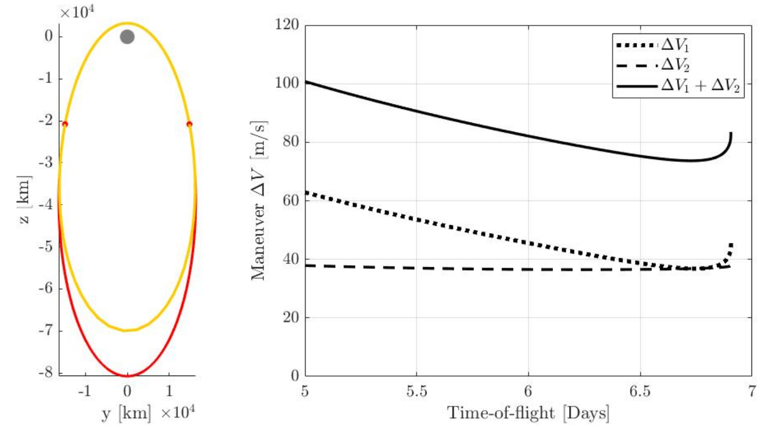

(a) (b)

Figure 5. Sample "exterior" transfer with a 24-hour phase shift behind across one revolution of the NRHO, (a) illustrated in the Earth-Moon rotating frame, (b) and the evolution of maneuver magnitude and time-of-flight along the solutions.

Because longer times-of-flight often yield a reduction in propellant costs, two-burn transfer families are constructed that span multiple revolutions of the NRHO. Consider a 12-hour phase shift backward in the NRHO that is achieved over two revolutions. A sample trajectory is illustrated in Figure 7(a), while the evolution of maneuver magnitude and time-of-flight is depicted in Figure 7(b). The transfer in Figure 7(a)

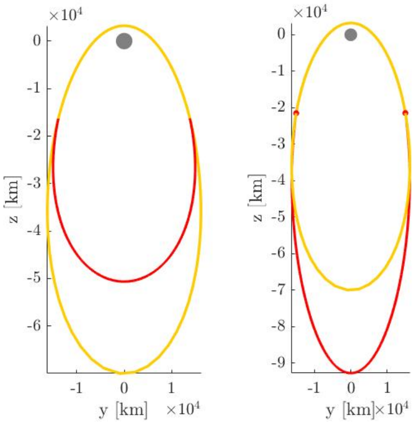

(a) (b)

Figure 6. Transfers with a 48-hour phase shift (a) ahead, i.e., an "interior" transfer, and (b) behind, i.e., an "exterior" transfer, in the NRHO, depicted in the Earth-Moon rotating frame.

has a flight duration of 12.5 days, and a cumulative maneuver magnitude of 16.6 m/s. The blue transfer from Figure 4(a) has approximately half the time-of-flight with twice the total maneuver cost than the transfer in Figure 7(a). A similar process is repeated for the 48-hour phase shift ahead case. Consider the red arc in Figure 8(a), where the time-of-flight is 10.2 days, and the maneuver cost is 69.7 m/s. The longer time-of-flight allows for more time for the spacecraft to drift from the reference NRHO. One challenge emerges in the subsequent revolutions prior to arrival back onto the NRHO. The intermediate revolution has perilune altitude of 827 km, which is lower than the 9:2 NRHO altitude in the CR3BP (1491 km). For a larger shift in phase, the trajectory may reduce the perilune altitude, which could interfere with operational altitude constraints.

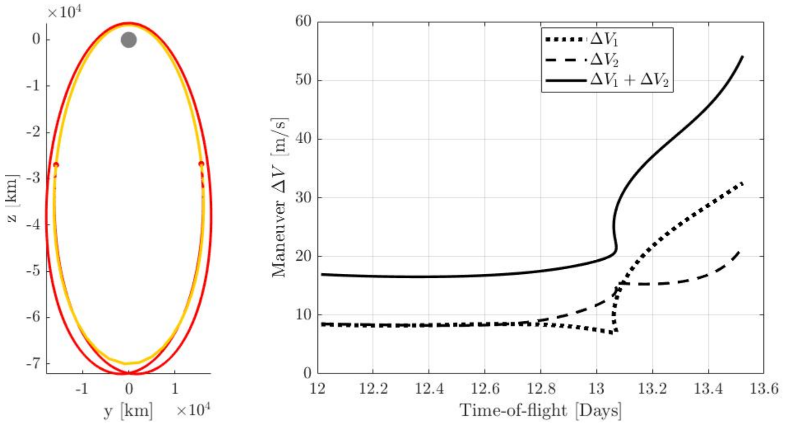

(a) (b)

Figure 7. Sample exterior transfer with a 24-hour phase shift behind across one revolution of the NRHO, (a) illustrated in the Earth-Moon rotating frame, (b) and the evolution of maneuver magnitude and time-of-flight along the solutions.

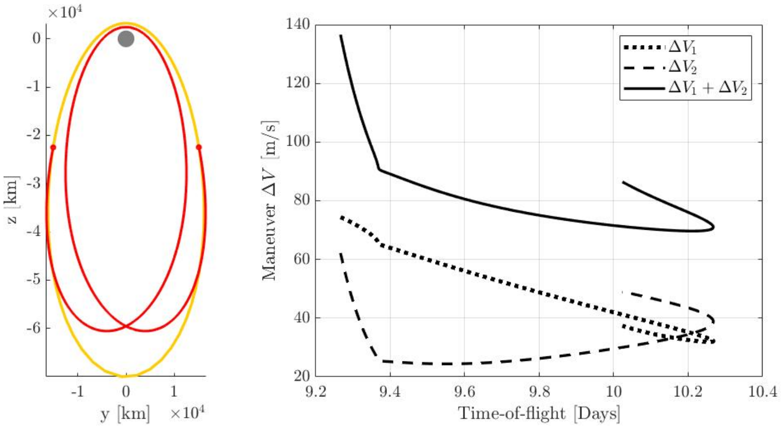

(a) (b)

Figure 8. Sample interior transfer with a 24-hour phase shift behind across one revolution of the NRHO, (a) illustrated in the Earth-Moon rotating frame, (b) and the evolution of maneuver magnitude and time-of-flight along the solutions.

Two-Burn Ephemeris Results

The transfers constructed in the CR3BP provide a basis for expected maneuver costs in the ephemeris model. A strategy to perform the two-burn rephase is implemented in FreeFlyer to assess maneuver costs given operational considerations, such as maneuver execution error and navigation error. A phase-shifted baseline is generated apriori to provide a state to target for the transfer arc and a set of stationkeeping targets once the rephase is completed. First, the revolution number and true anomaly along the nominal baseline are selected to determine the placement of Δv_1. Then, the phase shift duration is selected, defining the number of revolutions included in the transfer arc. Finally, the location of Δv_2 along the new baseline is defined in terms of osculating true anomaly. Then, the simulation is started and the spacecraft performs nominal stationkeeping until the rephase revolution is tripped. Once the rephase revolution is tripped, Δv_1 is targeted using a differential corrections process and executed. The simulation continues propagating the spacecraft for the time along the transfer arc, until Δv_2 is targeted and executed to arrive on the new NRHO phase. Finally, the spacecraft returns to performing stationkeeping using the new phase NRHO v_x and t_p targets. Each simulation finishes when the total number of revolutions reaches 56.

First, the example of a two-burn rephase is investigated where Δv_1 and Δv_2 occur on the same revolution. Performing the maneuvers on the same revolution reduces the time-of-flight and reduces that amount of errors that build up during the transfer arc; however, the Δv cost is higher compared to multi-revolution two-burn transfers. The phase that is targeted is 12 hours behind the nominal baseline NRHO, so the transfer is classified as an exterior transfer. The corresponding CR3BP solution is found in Figure 4(a), using a 4.7 day time-of-flight. This time-of-flight corresponds to a true anomaly of $160°$ for the location of Δv_1 and a true anomaly of $200°$ for the location of Δv_2. To ensure various uncertainties and all the Earth-Moon geometries are captured in the ephemeris model, 50 Monte Carlo trials are performed where Δv_1 is executed on nine different revolutions of the nominal baseline NRHO, since the Earth-Moon geometry repeats for every nine revolutions of the NRHO. The nine 50-trial simulations are performed and the mean/min/max maneuver costs for each Monte Carlo simulation are plotted in Figure 9 as a function of Δv_1 revolution number. The CR3BP maneuver cost is plotted in Figure 9 in gold, as well. Note that the ephemeris model results oscillate around the CR3BP solution. Thus, the maneuvers computed in the CR3BP provide a good approximation of the maneuver costs that are present in the ephemeris model, for this example.

In addition to single revolution transfers, multi-revolution transfers are examined in a higher-fidelity model. Consider the same scenario, where a rephase to 12 hour behind is desired and locations of Δv_1 and Δv_2 are

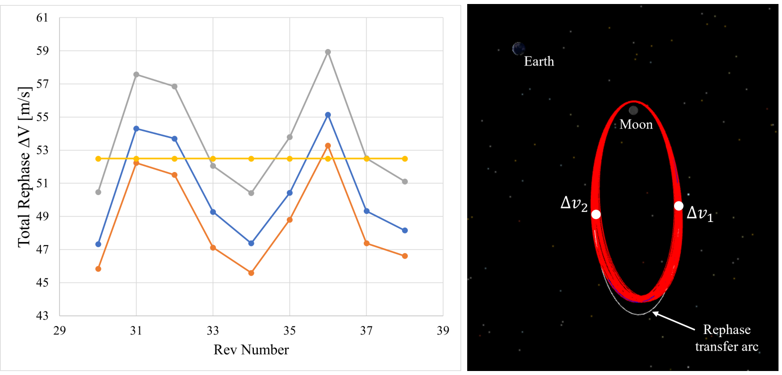

(a) (b)

Figure 9. (a) Mean (blue), minimum (orange), and maximum (grey) maneuver cost for the two-burn 12 hour behind rephase. The equivalent CR3BP maneuver cost is plotted in gold. (b) Example of a two-burn rephase in the ephemeris model.

at true anomalies of 160° and 200°, repsectively. However, a two revolution transfer is desired, where the transfer arc passes over perilune once before performing Δv_2 to arrive on the phase-shifted NRHO. The same stationkeeping strategies are performed before and after the rephase as were performed in the one revolution case. The same initial simulation setup is used in this scenario as the one revolution case. Revolutions 30-38 are selected to start the rephase transfer and execute Δv_1, where 50 Monte Carlo trials are simulated to assess this two-revolution transfer in the ephemeris model. The maneuver results from the nine simulations are plotted in Figure 10(a). Note that the total Δv for the two-revolution transfers are lower than for the one-revolution tranfers for all cases, indicating there is a correlation between time-of-flight and minimum Δv. The maneuver magnitude for 50 Monte Carlo trials is also plotted in Figure 10(b). The two large maneuvers correspond to Δv_1 and Δv_2 for the rephase transfer. Note that there is a high variation in the first orbit maintenance maneuver after the rephase is completed to clean up the errors accrued during the rephase transfer.

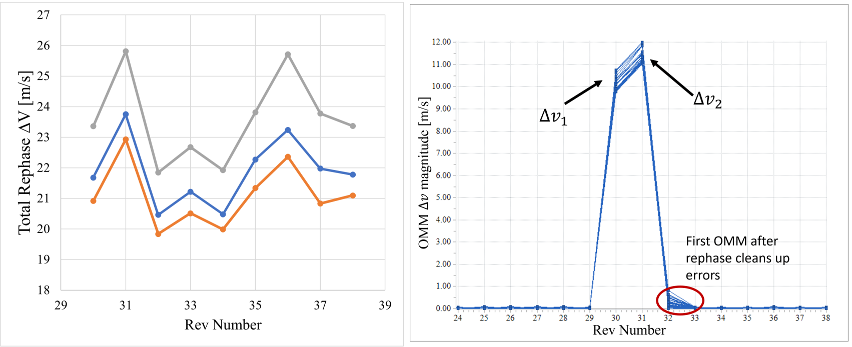

(a) (b)

Figure 10. (a) Mean (blue), minimum (Orange), and maximum (grey) maneuver cost for the two-burn 12 hour behind rephase using a 2 revolution transfer. (b) Maneuver magnitude as a function of rev number for 50 Monte Carlo trials using a two-burn rephase.

Four-Burn Rephasing Strategy

In addition to the two-burn rephasing strategy, a four-burn rephasing strategy is developed to leverage an intermediate orbit for rephasing. By leveraging an intermediate orbit, longer rephasing times are achieved for a maneuver cost similar to that of the two-burn rephase before, and the spacecraft has the ability to stationkeep in the intermediate orbit for longer rephasing times. A diagram of the four-burn rephasing is appears in Figure 11. The spacecraft departs the 9:2 NRHO along the orange arc, until it reaches the apolune of the intermediate orbit (black), then performs a second maneuver to arrive on the intermediate orbit. The spacecraft follows the intermediate orbit for n revolutions, then departs the intermediate orbit at apolune and returns to the 9:2 NRHO at the desired phase. Solutions are first examined in the CR3BP to understand the fundamental motion associated with this four-burn strategy. Using the symmetry properties present in the CR3BP, a targeting process is setup to target the transfer arc along with the intermediate orbit. The free-variable vector for the targeting problem is defined,

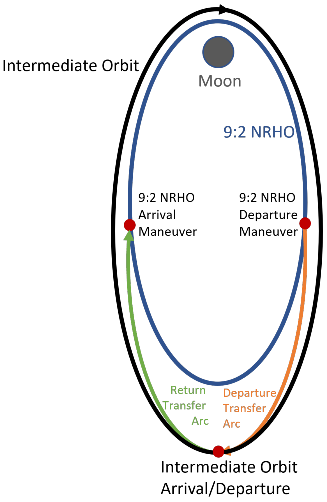

Figure 11. Four-maneuver rephase strategy diagram (not to scale).

$$\bar{X} = \begin{bmatrix} \Delta\bar{v}_1 & \Delta\bar{v}_2 & \bar{x}_T & t_T & \bar{x}_{\text{PO}} & t_{\text{PO}} & t_{\text{depart}} \end{bmatrix}^T \tag{11}$$

where $\Delta\bar{v}_1$ is the departure maneuver from the 9:2 NRHO onto the departure transfer arc, $\Delta\bar{v}_2$ is arrival maneuver on the intermediate orbit, $\bar{x}_T$ is the initial state on the departure transfer arc, t_T is the departure transfer arc time, $\bar{x}_{\text{PO}}$ is the apolune state of the intermediate periodic orbit, t_{PO} is the period of the intermediate periodic orbit, and t_{depart} is time since perilune on the 9:2 NRHO that Δv_1 is performed. Since the problem is symmetric about the xz-plane in the CR3BP, the return transfer arc and associated maneuvers are mirrored from the departure transfer arc across the xz-plane. The constraints for the problem are defined,

$$\bar{F} = \begin{bmatrix} \bar{r}_{9:2} - \bar{r}_T \\ \bar{v}_{9:2} + \Delta\bar{v}_1 - \bar{v}_T \\ \bar{r}^t_T - \bar{r}_{\text{PO}} \\ \bar{v}^t_T + \Delta\bar{v}_2 - \bar{v}_{\text{PO}} \\ p - ((nt_{\text{PO}} + 2t_T) - (mP_{9:2} - t_{\text{diff}}) \\ y_{\text{PO}} \\ \dot{x}_{\text{PO}} \\ \dot{z}_{\text{PO}} \\ y^t_{\text{PO}} \\ \dot{x}^t_{\text{PO}} \\ \dot{z}^t_{\text{PO}} \\ F_{opt} \end{bmatrix} \tag{12}$$

where $\bar{r}_{9:2}$ and $\bar{v}_{9:2}$ are the departure position and velocity on the 9:2 NRHO, $\bar{r}_T$ and $\bar{v}_T$ is position and velocity at the beginning of the departure transfer arc, $\bar{r}^t_T$ and $\bar{v}^t_T$ is position and velocity at the end of the departure transfer arc, n is number of revolutions the spacecraft will take around the intermediate orbit, y_{PO}, $\dot{x}_{\text{PO}}$, and $\dot{z}_{\text{PO}}$ are components of the state vector at the apolune state of the intermediate periodic orbit, y^t_{PO}, $\dot{x}^t_{\text{PO}}$, and $\dot{z}^t_{\text{PO}}$ are components of the state vector at the perilune state of the intermediate periodic orbit, t_{diff} time between the departure location and the arrival location along the 9:2 NRHO, and F_{opt} is the optimality constraint defined in Equation (6). Note that there are 20 constraints and 21 free variables, so a family of Δv-optimal solutions exists for various t_{depart} times along the 9:2 NRHO. The cost function used in the F_{opt} constraint is defined,

$$f = 2|\Delta\bar{v}_1| + 2|\Delta\bar{v}_2| \tag{13}$$

To construct the family of optimal solutions for particular value p, a pseudo-arclength continuation method is leveraged. Examples of families of transfers in the CR3BP for $p = 1.0$, $p = 2.0$, $p = 3.0$, and $p = 4.0$ days are plotted in Figure 12, colored by the total Δv required for the rephase. The blue dots indicate where Δv_1 is performed to depart the original phase on the 9:2 NRHO, the red dots indicate where Δv_2 and Δv_3 are performed to arrive and depart the intermediate orbit, respectively, and the orange dots indicate where Δv_4 is performed to arrive on the new phase of the 9:2 NRHO. Note that for each family of four-burn rephases, the intermediate orbit remains similar for a given rephase duration. The total Δv is plotted as a function of the osculating true anomaly along the NRHO where Δv_1 is initiated in Figure 13(a). Note that the curves in Figure 13(a) correspond to a transfer that performs one revolution around the intermediate orbit. The asymptotes at true anomalies less than 180° correspond to solutions with very short times-of-flight for the transfer segements to and from the intermediate orbit. The intermediate orbits associated with those high Δv cases also have high perilune altitudes, as indicated by the plot in Figure 13(b), which plots the total rephase Δv as a function of perilune altitude of the intermediate orbit.

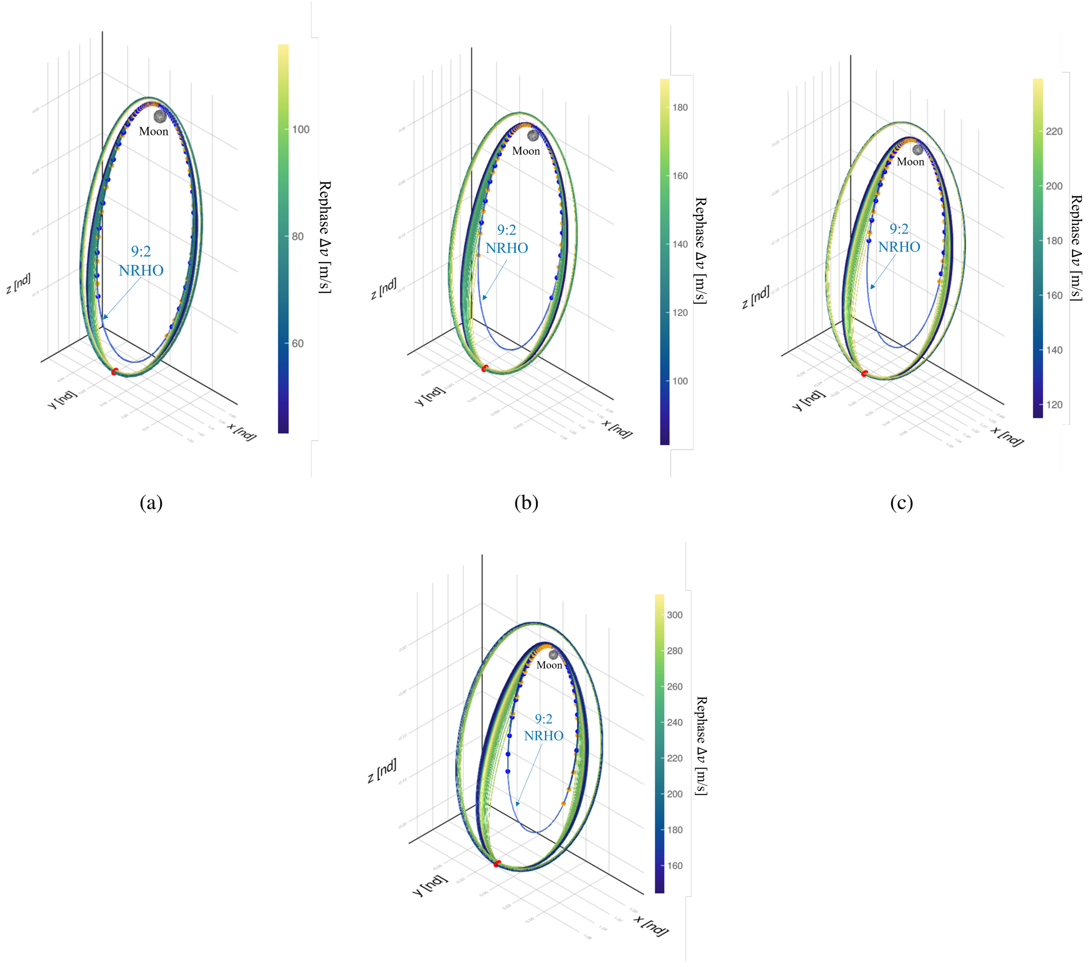

(a)

(b)

(c)

(d)

Figure 12. A family of local Δv-optimal four-burn rephase transfers in the CR3BP, where (a) $p = 1.0$ day, (b) $p = 2.0$ days, (c) $p = 3.0$ days, (d) $p = 4.0$ days.

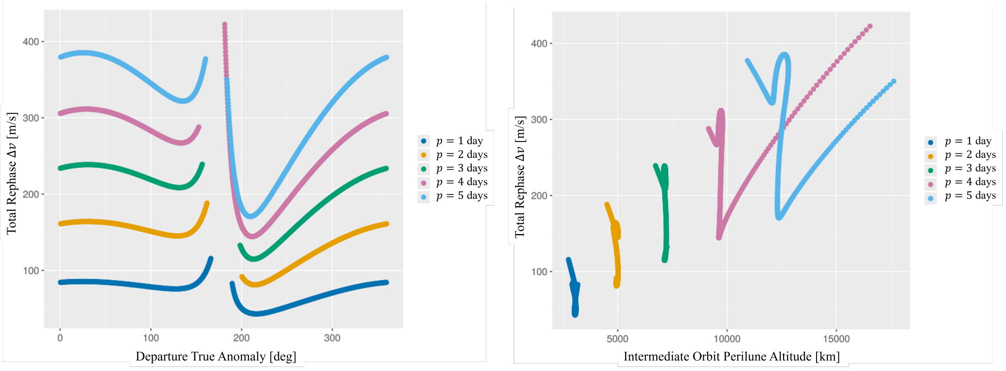

(a)

(b)

Figure 13. (a) Total Δv plotted as a function of the true anomaly where Δv_1 is initiated. (b) Total Δv plotted as a function of the intermediate orbit perilune altitude. Each of the curves represent a different rephase duration.

Four-Burn Ephemeris Results

To ensure the trajectories constructed in the CR3BP are feasible in a higher-fidelity model, a simulation in a Sun-Earth-Moon ephemeris model is performed for the four-burn rephase. The targeting process differs from the process formulated for the CR3BP; however, information from the results from the CR3BP are incorporated to inform the initial guess in the ephemeris model. Before executing the ephemeris simulation, several steps are required. First, a subset of the L_2 southern halo orbit family is constructed in the CR3BP. This subset includes the NRHO region of the halo family and the perilune altitudes in the subset range from 0.0 km to 31,000 km. The information associated with this subset of orbits is used to generate a reference trajectory in the Sun-Earth-Moon ephemeris model in the rephasing simulation. Next, a phase-shifted 9:2 NRHO long-term baseline trajectory is generated using the methods summarized by Zimovan-Spreen, et al[11] and provides orbit maintenance targets for stationkeeping after four-burn rephase is completed. Lastly, the true anomaly and revolution number along the original 9:2 NRHO baseline trajectory are selected to initiate the first maneuver of the rephasing. Using the input true anomaly, there is corresponding periodic orbit in the CR3BP selected. This selected orbit corresponds to the intermediate orbit that delivers the optimal rephasing Δv in the CR3BP. Using the information from this optimal intermediate CR3BP periodic orbit, a transition process is leveraged to produce this orbit in the Sun-Earth-Moon ephemeris model. Since the CR3BP periodic NRHO does not remain exactly periodic in the Sun-Earth-Moon ephemeris model, a reference trajectory for the intermediate rephasing orbit is constructed. To construct the intermediate reference trajectory, a base epoch is first selected. In the ephemeris model, the period of the reference trajectory is not always exactly equal to the period computed in the CR3BP; therefore, an equation is used to compute the base epoch, τ_b, of the intermediate trajectory,

$$\tau_b = \frac{\tau_{\theta_1^*} + \tau_{\theta_2^*}}{2} - \frac{t_{\mathrm{PO}}}{2} \tag{14}$$

where $\tau_{\theta_1^*}$ is the epoch at the departure location along the original 9:2 NRHO baseline, $\tau_{\theta_2^*}$ is the epoch at the arrival location along the destination phase-shifted 9:2 NRHO baseline, and t_{PO} is the period of the intermediate CR3BP orbit, defined in Equation (4). Using this base epoch, ten revolutions of an intermediate reference trajectory are constructed using a multiple-shooting technique, summarized by Zimovan.[12] Ten revolutions are used to ensure the reference trajectory maintains its geometry in the ephemeris model. The diagram in Figure 14 illustrates how the epochs are selected relative to the perilunes on each revolution of the orbit. The base epoch, τ_b, is assigned to the perilune of revolution 5, while epochs associated with perilunes on previous and future revolutions are a multiple of the CR3BP orbit period plus the base epoch.

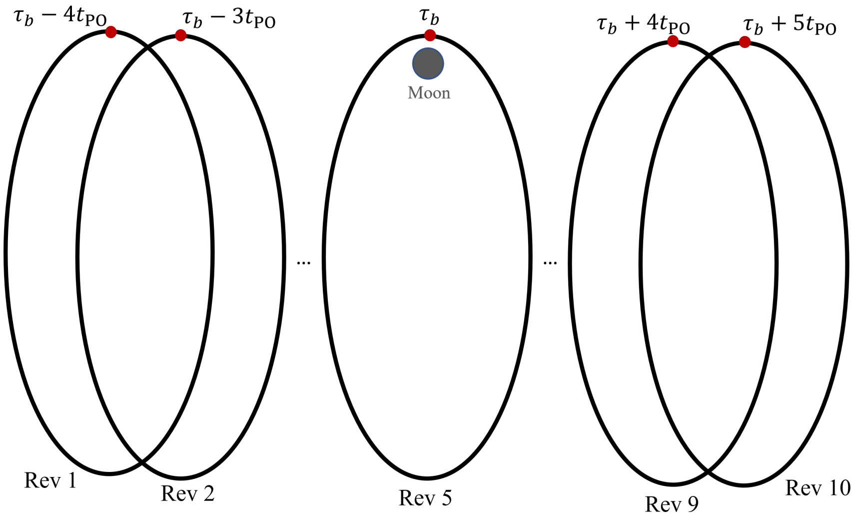

Figure 14. Diagram of the epoch assignment at perilune of each revolution of the intermediate reference trajectory.

Once the intermediate reference trajectory is constructed, the nominal stationkeeping is simulated, as summarized by Davis et al.,[13] until the rephase is triggered in the simulation. A workflow of the rephase targeting process is illustrated in Figure 15. Once the epoch of the first rephase maneuver is triggered at $\tau_{\theta_1^*}$, a differential corrector is used to target the apolune state on the intermediate reference trajectory using Δv_1 and Δv_2 to achieve those targets. Once the conditions of the intermediate orbit apolune are achieved, the state is propagated to the next apolune. Then, a differential corrector is used to target the state on the new baseline 9:2 NRHO at the epoch $\tau_{\theta_2^*}$. Once the targeting is completed, the maneuvers are executed and the simulation returns to the nominal orbit maintenance strategy for the remainder of the simulation using the orbit maintenance targets from the phase shifted baseline NRHO.

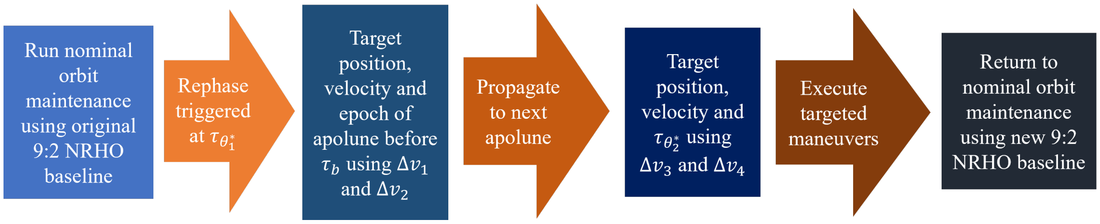

Figure 15. Rephase targeting process.

The results of these rephasing strategies are validated in a higher fidelity ephemeris model using a Monte Carlo analysis. Stationkeeping maneuver execution errors, navigation errors, SRP errors, and insertion errors are included in each Monte Carlo trial to validate solutions constructed in the CR3BP. The implementation and quantification of these errors are summarized by Davis et al.[13] The simulation is run for 1 year and the first rephase maneuver is initiated along revolution 13-21 of the original 9:2 NRHO baseline. Initiating the rephasing maneuver on different revolutions provides insight into how the Sun-Earth-Moon geometry affects the rephasing transfer strategy. Additionally, selecting the revolution to initiate the rephase must be a sufficient amount of time after the beginning of the simulation such that the errors imparted during the nominal stationkeeping are represented. Consider a scenario where a two-day rephase is required, i.e., the vehicle needs to shift to a phase that is two days behind its current phase. Simulation is setup such that the first departure maneuver along the original phase occurs at $\theta^* = 120°$ and the arrival true anomaly along the phase shifted NRHO is $\theta^* = 240°$. These true anomaly values were selected as a representative example. The intermediate NRHO chosen for the rephase has a period of 7.68 days, approximately 1.12 days longer than the 9:2 NRHO. In Figure 16(a), an example trial of the trajectory is rendered in the Earth-Moon rotating frame, as well as the locations of the Δv's. The mean total maneuver magnitude of the rephase is plotted as a function of the Δv_1 revolution number in Figure 16(b). The Δv calculated in the CR3BP that serves as the initial guess is included in Figure 16(b) as well, plotted in gold. Note that the mean Δv changes depending on the revolution number, and the Δv computed in the CR3BP remains near the average Δv computed across all revolutions in the FreeFlyer simulation.

The four-burn rephase strategy is also applied to transitioning between eclipse-free NRHO baseline trajectories. Zimovan-Spreen, et al. summarize a process to generate eclipse-free long-term baseline NRHO trajectories for the Gateway.[11] Scenarios may arise that require the Gateway to shift phase and target a different, eclipse free baseline 9:2 NRHO. Zimovan-Spreen, et al. discuss a method to leverage a modified orbit maintenance strategy to achieve the rephase, but operation constraints may require a shorter time-of-flight to accomplish the rephase. Subsequently, the four-burn rephase strategy is applied to this problem to demonstrate that shifting to a new, eclipse-free phase NRHO is possible. First, an eclipse-free baseline is generated that provides the orbit maintenance targets for the post-rephase stationkeeping. Next, an initial guess is generated in the CR3BP to determine the intermediate orbit and the proper θ_1^* and θ_2^* values. The initial guess selected possesses $\theta_1^* = 220°$ and $\theta_2^* = 140°$, and the period of the intermediate orbit is 8.49 days. Similar to the 2 day rephase example, 50 Monte Carlo trials are performed on nine different revolutions where the rephase is initiated. The maneuver statistics from the Monte Carlo simulations are plotted in Figure 17(b) as well as the maneuver cost computed in the CR3BP colored in gold. This rephasing strategy takes on the order of 2.5 weeks to transition from one eclipse-free NRHO phase to another, whereas the modified orbit mainte-

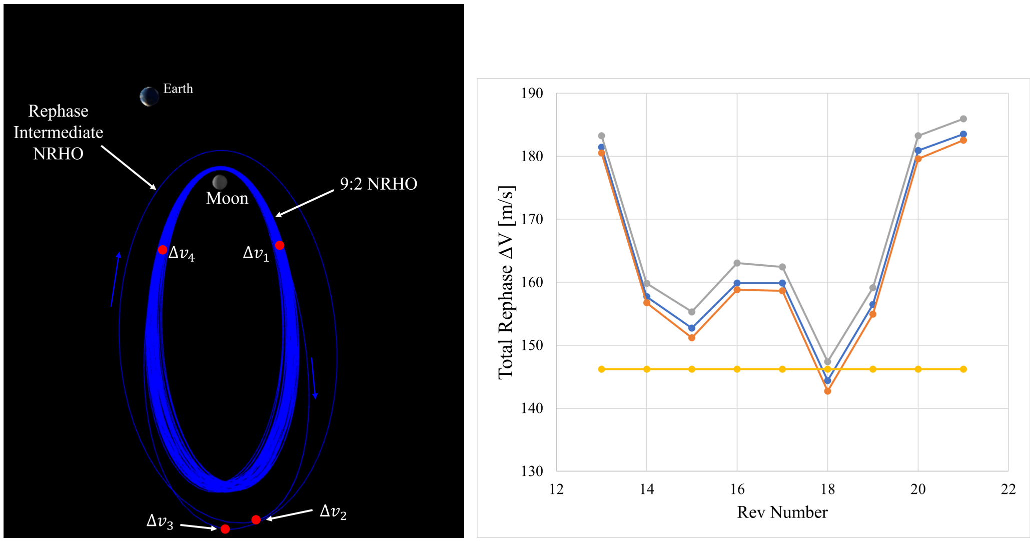

(a) (b)

Figure 16. (a) Example simulation of a 2 day rephase in the ephemeris model, rendered in the Earth-Moon rotating frame. (b) The mean (blue), min (orange), and max (grey) maneuver magnitudes when the rephase is performed on nine different revolutions of the NRHO. The gold line represents the CR3BP solution used as the initial guess for the Monte Carlo simulation.

nance strategy accomplishes the phase shift over several months; however, a shorter time-of-flight four-burn phase shift requires more propellant. Multiple rephasing strategies provide flexibility for mission scenarios that may be encountered that require shorter times-of-flight or limited propellant usage.

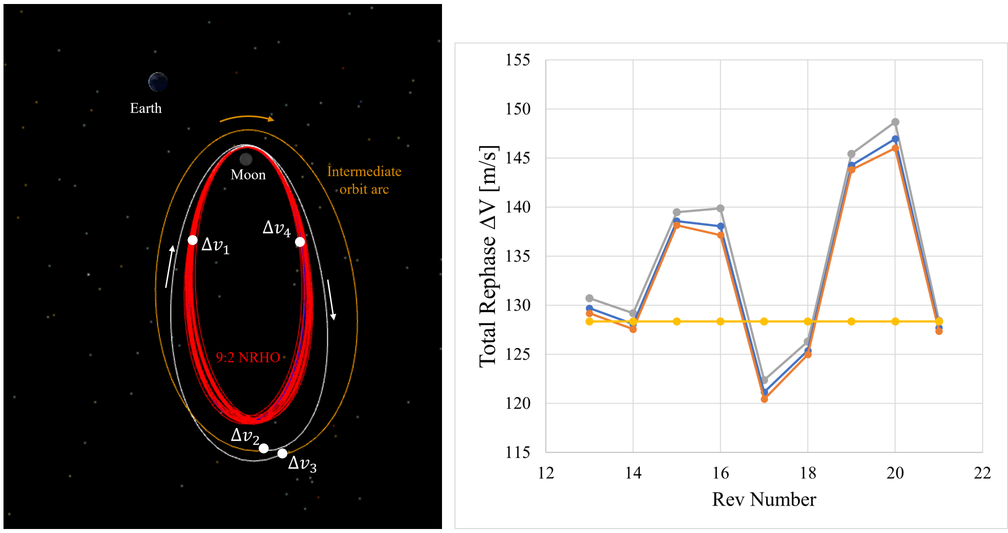

(a) (b)

Figure 17. (a) Example simulation of a rephase between two eclipse-free NRHO baselines in the ephemeris model, rendered in the Earth-Moon rotating frame. (b) The mean (blue), min (orange), and max (grey) maneuver magnitudes when the rephase is performed on nine different revolutions of the NRHO. The gold line represents the maneuver cost computed in the CR3BP.

CONCLUDING REMARKS

Overall, this investigation summarizes two rephasing strategies in the 9:2 NRHO. The first strategy uses two maneuvers and a single transfer arc to shift the phase along the NRHO. The second strategy leverages an intermediate orbit and four maneuvers to rephase a vehicle in the NRHO. The advantage of the four-burn rephase is that longer rephasing times can be achieved. Additionally, in the event of a contingency, the intermediate orbit can be maintained using a similar stationkeeping strategy as the 9:2 NRHO, as demonstrated by Davis et al.[14] An optimization and continuation process is summarized for each of these methods and results are validated through Monte Carlo simulations in the Sun-Earth-Moon ephemeris model. Additionally, this analysis focused on applications related to Gateway operations, but is extendable to analyses associated with other libration point orbits. Ultimately, effective rephasing strategies make operations in the NRHO more flexible to changing mission constraints and off-nominal scenarios.

ACKNOWLEDGEMENTS

The authors would like to thank Rolfe Power and Damennick Henry for insightful discussions about the optimization method paired with pseudo-arclength continuation as well as help with development of the proof as it relates to the method of Lagrange multipliers. The authors would also like to thank David Lee for introducing the concept for the four-burn rephasing strategy.

APPENDIX: EQUIVALENCE OF GRADIENT CONSTRAINT TO METHOD OF LAGRANGE MULTIPLIERS

Consider a generic optimization problem to minimize or maximize some scalar cost function $f(\bar{X})$, subject to the constraint $\bar{F}(\bar{X}) = 0$. Suppose that $\bar{X}$ is an $n \times 1$ vector and $\bar{F}(\bar{X})$ is a $(n-l) \times 1$ vector. The objective of this appendix is to demonstrate the equivalence of the formulated gradient constraint

$$\nabla f(\bar{X}) \bullet \text{null}(D\bar{F}(\bar{X})) = 0 \tag{15}$$

with the method of Lagrange multipliers in an approachable manner, where $D\bar{F}(\bar{X})$ is the Jacobian of $\bar{F}$ with respect to $\bar{X}$. A generalization will also be introduced for the cases when the null space of $D\bar{F}(\bar{X})$ has a dimension greater than one.

Intuitively, Equation (15) can be viewed as the definitional requirement for an critical point of $f(\bar{X})$. Consider $S = \{\bar{X} | \bar{F}(\bar{X}) = 0\}$. This constraint manifold defines the collection feasible solutions. Near any given feasible solution, $\bar{X}^* \in S$, a local approximation for $\bar{F}(\bar{X})$ can be written as

$$\bar{F}(\bar{X}) \approx D\bar{F}(\bar{X}^*)(\bar{X} - \bar{X}^*) = D\bar{F}(\bar{X}^*)\delta\bar{X}, \tag{16}$$

since $\bar{F}(\bar{X}^*) = 0$ by assumption. Notably, the constraint manifold S can then be locally approximated near $\bar{X}^*$ as $S \approx \{\bar{X} | D\bar{F}(\bar{X}^*)\delta\bar{X} = 0\}$. It is clear from this approximation that $\delta\bar{X} \in \text{null}(D\bar{F}(\bar{X}^*))$ defines a tangent vector to S at $\bar{X}^*$. The collection of all such tangent vectors is, then, the nullspace of $D\bar{F}(\bar{X}^*)$. Since $\nabla f(\bar{X})$ defines a direction of maximal change in the objective function, Equation (15) can be interpreted as requiring that the component of the change in the cost function along the constraint manifold is zero. This is the requirement for an critical point that also satisfies the specified constraint function.

In the method of Lagrange multipliers, an optimal solution is computed by introducing $n - l$ additional unknowns in the form of the Lagrange multipliers, $\bar{\lambda}$, and simultaneously solving the $2n - l$ equations defined by

$$\bar{F}(\bar{X}) = 0 \tag{17}$$

$$\nabla f(\bar{X}) + \bar{\lambda}^T D\bar{F}(\bar{X}) = 0. \tag{18}$$

There are several ways to prove the equivalence of the method of Lagrange multipliers with the optimality constraint in Equation (15). In this appendix, an accessible proof that avoids concepts from differential geometry is employed. Specifically, the following proposition is considered.

Proposition 1 *There are unique locally optimal* $\bar{X}_{opt}$ *and* $\bar{\lambda}_{opt}$ *such that Equations* (17) *and* (18) *are satisfied if and only if* $\bar{F}(\bar{X}_{opt}) = 0$ *and* $\nabla f(\bar{X}_{opt})$ *is orthogonal to all vectors in the nullspace of* $D\bar{F}(\bar{X}_{opt})$*.*

Proof It will first be shown that if such $\bar{X}_{opt}$ and $\bar{\lambda}_{opt}$ exist, then $\nabla f(\bar{X}_{opt})$ is orthogonal to all vectors in the nullspace of $D\bar{F}(\bar{X}_{opt})$. Consider the singular value decomposition of the matrix $D\bar{F}(\bar{X}_{opt})$, i.e.,

$$D\bar{F}(\bar{X}_{opt}) = U\Sigma V^T \tag{19}$$

where

$$\begin{aligned} U &= \begin{bmatrix} \bar{U}_1 & \cdots & \bar{U}_{n-l} \end{bmatrix} \\ V &= \begin{bmatrix} \bar{V}_1 & \cdots & \bar{V}_{n-l} & \cdots & \bar{V}_n \end{bmatrix} \\ \Sigma &= \begin{bmatrix} \sigma_1 & 0 & 0 & \cdots & 0 & 0_{1\times l} \\ 0 & \sigma_2 & 0 & \cdots & 0 & 0_{1\times l} \\ 0 & 0 & \sigma_3 & \cdots & 0 & 0_{1\times l} \\ \vdots & \vdots & \vdots & \ddots & \vdots & \vdots \\ 0 & 0 & 0 & \cdots & \sigma_{n-l} & 0_{1\times l} \end{bmatrix}. \end{aligned}$$

Note that the last l columns of V form a mutually orthogonal basis for null$(D\bar{F}(\bar{X}_{opt}))$. Denote $\mathcal{N} = \begin{bmatrix} \bar{V}_{n-l+1} & \cdots & \bar{V}_n \end{bmatrix}$. Multiplying both sides of Equation (18) by $\mathcal{N}$ yields

$$\nabla f(\bar{X}_{opt})\mathcal{N} = 0. \tag{20}$$

Since any vector in the null space of $D\bar{F}(\bar{X}_{opt})$ can be written as $\bar{N} = \mathcal{N}\alpha$, it is clear that $\nabla f(\bar{X}_{opt})\bar{N} = 0$ for any $\bar{N}$, proving that the existence of $\bar{X}_{opt}$ and $\bar{\lambda}_{opt}$ such that Equations (17) and (18) are satisfied implies that $\nabla f(\bar{X}_{opt})$ is orthogonal to all vectors in the nullspace of $D\bar{F}(\bar{X}_{opt})$. To demonstrate the converse statement, note that Equation (17) is trivially satisfied by the assumptions on $\bar{X}_{opt}$ and consider the rearranged transpose of Equation (18)

$$(D\bar{F}(\bar{X}))^T\bar{\lambda} = -(\nabla f(\bar{X}))^T. \tag{21}$$

The existence of unique $\bar{\lambda}_{opt}$ satisfying Equation (21) will be demonstrated by constructing the vector. Since $\bar{\lambda}_{opt}$ is an $(n-l)\times 1$ column vector, it can uniquely be expressed as a linear combination of the $\bar{U}_i$, i.e.,

$$\bar{\lambda}_{opt} = U\bar{c}. \tag{22}$$

From the stated assumptions on $\nabla f(\bar{X}_{opt})$, it is possible to write

$$(\nabla f(\bar{X}_{opt}))^T = \sum_{i=1}^{n-l} \beta_i \bar{V}_i,$$

since this gradient exists in the orthogonal complement of the nullspace of $D\bar{F}(\bar{X}_{opt})$. Noting that $(D\bar{F}(\bar{X}_{opt}))^T = V\Sigma^T U^T$, it can be seen that for a unique $\bar{\lambda}_{opt}$ to exist, it must be true that

$$V\Sigma^T\bar{c} = -\sum_{i=1}^{n-l} \beta_i \bar{V}_i. \tag{23}$$

where $\bar{c}$ is an unique vector of dimension $n-l$. Noting the form of $V\Sigma^T = \begin{bmatrix} \sigma_1\bar{V}_1 & \cdots & \sigma_{n-l}\bar{V}_{n-l} \end{bmatrix}$, this relationship is equivalent to

$$\sum_{i=1}^{n-l} c_i\sigma_i\bar{V}_i = -\sum_{i=1}^{n-l} \beta_i\bar{V}_i. \tag{24}$$

Since the $\bar{V}_i$ are mutually orthogonal (from their construction via the singular value decomposition of $D\bar{F}(\bar{X}_{opt})$), it can be seen that

$$c_i = -\beta_i/\sigma_i, \tag{25}$$

which allows for the unique determination of $\bar{\lambda}_{opt}$ from Equation (22). This demonstrates the converse statement and shows the desired equality Q.E.D.

Proposition 1 indicates that the method employed in this investigation for computing optimal solutions can be generalized to an l-dimensional nullspace of $D\bar{F}$ by introducing l additional constraints that ensure that $\nabla f(\bar{X})$ is in the orthogonal complement of $D\bar{F}(\bar{X})$. This condition can be enforced, for example, by requiring $\mathcal{N}^T(\nabla f(\bar{X}))^T = 0_{l\times 1}$.

REFERENCES

[1] K. Hambleton, T. Fairley, and L. Cheshier, "Splashdown! NASA's Orion Returns to Earth After Historic Moon Mission," *web*, Dec. 2022. https://www.nasa.gov/press-release/splashdown-nasa-s-orion-returns-to-earth-after-historic-moon-mission.

[2] F. Khoury and K. Howell, "Orbital Rendezvous and Spacecraft Loitering in the Earth-Moon System," *AAS/AIAA Astrodynamics Specialist Conference*, Virtual, Aug. 2020.

[3] C. G. Sandel and R. Sood, "Low-Thrust Rendezvous and Proximity Operations in a Near Rectilinear Halo Orbit," *33rd AAS/AIAA Space Flight Mechanics Meeting*, Austin, Texas, Jan. 2023.

[4] D. C. Davis, E. M. Zimovan-Spreen, S. T. Scheuerle, and K. C. Howell, "Debris Avoidance and Phase Change Maneuvers in Near Rectilinear Halo Orbits," *44th Annual AAS Guidance, Navigation, and Control Conference*, Breckenridge, Colorado, Feb. 2022.

[5] E. Blazquez, L. Beauregard, S. Lizy-Destrez, F. Ankersen, and F. Capolupo, "Rendezvous design in a cislunar near rectilinear halo orbit," *Aeronautical Journal*, Vol. 124, Dec. 2020, pp. 821–837.

[6] G. Bucchioni, S. Lizy-Destrez, T. Vaujour, V. Thoraval, L. Rouverand, and C. Silva, "Phasing with near rectilinear Halo orbits: Design and comparison," Vol. 71, Mar., pp. 2449–2466.

[7] V. Szebehely, *The Theory of Orbits: The Restricted Problem of Three Bodies*. New York, New York: Academic Press, Inc, 1967.

[8] C. H. Acton, *Ancillary Data Services of NASA's Navigation and Ancillary Information Facility*, Jan. 1996. https://naif.jpl.nasa.gov/naif/.

[9] H. B. Keller, *Numerical Methods for Two-Point Boundary-Value Problems*. Dover Publications, 1992.

[10] E. J. Doedel, V. A. Romanov, R. C. Paffenroth, H. B. Keller, D. J. Dichmann, J. Galán-Vioque, and A. Vanderbauwhede, "Elemental Periodic Orbits Associated with the Libration Points in the Circular Restricted 3-Body Problem," *International Journal of Bifurcation and Chaos*, Vol. 17, No. 8, 2007, pp. 2625–2677, 10.1142/S0218127407018671.

[11] E. Zimovan-Spreen, S. Scheuerle, B. McCarthy, D. Davis, and K. Howell, "Baseline Orbit Generation for Near Rectilinear Halo Orbits," *AAS/AIAA Astrodynamics Specialist Conference*.

[12] E. M. Zimovan, "Characteristics and Design Strategies for Near Rectilinear Halo Orbits within the Earth-Moon System," M.S. Thesis, Purdue University, West Lafayette, Indiana, Aug. 2017.

[13] D. C. Davis, S. T. Scheuerle, D. A. Williams, F. S. Miguel, E. M. Zimovan-Spreen, and K. C. Howell, "Orbit Maintenance Burn Details for Spacecraft in a Near Rectilinear Halo Orbit," *AAS/AIAA Astrodynamics Specialist Conference*.

[14] D. C. Davis, S. M. Phillips, K. C. Howell, S. Vutukuri, and B. P. McCarthy, "Stationkeeping and Transfer Trajectory Design for Spacecraft in Cislunar Space," *AAS/AIAA Astrodynamics Specialist Conference*, Stevenson, Washington, Aug. 2017.